

## Compact Thermal-Diffusivity-Based Temperature Sensors in 40-nm CMOS for SoC Thermal Monitoring

Sönmez, Uğur; Sebastiano, Fabio; Makinwa, Kofi A.A.

**DOI**

[10.1109/JSSC.2016.2646798](https://doi.org/10.1109/JSSC.2016.2646798)

**Publication date**

2017

**Document Version**

Accepted author manuscript

**Published in**

IEEE Journal of Solid State Circuits

**Citation (APA)**

Sönmez, U., Sebastiano, F., & Makinwa, K. A. A. (2017). Compact Thermal-Diffusivity-Based Temperature Sensors in 40-nm CMOS for SoC Thermal Monitoring. *IEEE Journal of Solid State Circuits*, 52(3), 834-843. Article 7835088. <https://doi.org/10.1109/JSSC.2016.2646798>

**Important note**

To cite this publication, please use the final published version (if applicable). Please check the document version above.

**Copyright**

Other than for strictly personal use, it is not permitted to download, forward or distribute the text or part of it, without the consent of the author(s) and/or copyright holder(s), unless the work is under an open content license such as Creative Commons.

**Takedown policy**

Please contact us and provide details if you believe this document breaches copyrights. We will remove access to the work immediately and investigate your claim.

# Compact Thermal-Diffusivity- Based Temperature Sensors in 40-nm CMOS for SoC Thermal Monitoring

Uğur Sönmez, Fabio Sebastiano and Kofi A.A. Makinwa  
Electronic Instrumentation Lab / DIMES  
Delft University of Technology  
Delft, The Netherlands

Email: {u.sonmez, f.sebastiano}@tudelft.nl  
Phone: +31648966870  
Contact Address: Mekelweg 4  
Delft, The Netherlands

***Abstract***— An array of temperature sensors based on the thermal diffusivity (TD) of bulk silicon has been realized in a standard 40-nm CMOS process. In each TD sensor, a highly-digital VCO-based  $\Sigma\Delta$  ADC digitizes the temperature-dependent phase-shift of an electro-thermal filter (ETF). A phase calibration scheme is used to cancel the ADC's phase offset. Two types of ETF were realized, one optimized for accuracy and one optimized for resolution. Sensors based on the accuracy-optimized ETF achieved a resolution of  $0.36\text{ }^{\circ}\text{C}$  (rms) at  $1\text{ kSa/s}$ , and inaccuracies of  $\pm 1.4\text{ }^{\circ}\text{C}$  ( $3\sigma$ , uncalibrated) and  $\pm 0.75\text{ }^{\circ}\text{C}$  ( $3\sigma$ , room-temperature calibrated) from  $-40$  to  $125\text{ }^{\circ}\text{C}$ . Sensors based on the resolution-optimized ETFs achieved an improved resolution of  $0.21\text{ }^{\circ}\text{C}$  (rms), and inaccuracies of  $\pm 2.3\text{ }^{\circ}\text{C}$  ( $3\sigma$ , uncalibrated) and  $\pm 1.05\text{ }^{\circ}\text{C}$  ( $3\sigma$ , room-temperature calibrated). The sensors draw  $2.8\text{ mA}$  from supply voltages as low as  $0.9\text{ V}$ , and occupy only  $1650\text{ }\mu\text{m}^2$ , making them some of the smallest smart temperature sensors reported to date, and well suited for thermal monitoring applications in systems-on-chip (SoC).

## I. INTRODUCTION

Today, microprocessors and other systems-on-chip (SoCs) employ billions of transistors that can switch at GHz rates. As a result, they can get hot enough to degrade their performance and even cause permanent damage. To avoid this, thermal management algorithms, driven by information from on-chip temperature sensors, slow them down or even shut them off when temperatures near reliability limits. To account for sensor errors, however, such algorithms must incorporate an appropriate safety margin. Given that the thermal resistance of a well-designed heat sink may be as low as  $0.5\text{ }^{\circ}\text{C}/\text{W}$ , a  $5\text{-}^{\circ}\text{C}$  margin corresponds to  $10\text{ W}$  of unused power [1]. Since a typical microprocessor dissipates less than  $100\text{ W}$ , this represents a significant loss of computing performance, and thus motivates the design of accurate temperature sensors. In multi-core microprocessors, substantial thermal gradients and hot spots may occur, whose location is a dynamic function of workload. Thus, multiple on-chip temperature sensors are required, both to ensure reliability and to optimally spread the workload over different cores [2].

Since the location of hot spots cannot be easily predicted at design time, on-chip sensors must be small enough to be deployed in large numbers (up to 44 in modern microprocessors [3]), and for their position in the layout to be flexibly moved, even at a late stage of the development [2]. Accuracy requirements must be satisfied while minimizing the calibration effort, which could otherwise significantly increase manufacturing costs, especially when tens of sensors per chip are involved. The greatest accuracy is required around the reliability limit, with typical specifications being  $\pm 1\text{ }^{\circ}\text{C}$  at  $70\text{ }^{\circ}\text{C}$ , and only  $\pm 3\text{ }^{\circ}\text{C}$  at  $50\text{ }^{\circ}\text{C}$  [2]. In addition, to properly detect thermal transients with slopes as high as  $0.5\text{ }^{\circ}\text{C}/\text{ms}$  [2], sensor resolution must be significantly less than  $0.5\text{ }^{\circ}\text{C}$ , even with measurement times as short as  $1\text{ ms}$ .

Most on-chip CMOS temperature sensors are currently based on parasitic PNPs thanks to their relatively simple design and good energy efficiency. When implemented in nanometer

CMOS, however, it has been shown that their inaccuracy is limited to only a few degrees Celsius, even after trimming [2,4,5]. Parasitic NPNs achieve better performance [6][28], but are not available in baseline CMOS processes. Moreover, the base-emitter voltages of BJTs is about 0.7 V at room temperature, which makes it quite challenging to operate them from today's 1-V supplies. Other types of temperature sensors, e.g. based on resistors [7], or MOS transistors [8,9], also exhibit poor inaccuracy when implemented in nanometer CMOS, and so must be combined with expensive multi-point temperature calibration.

As an alternative, the thermal diffusivity (TD) of bulk silicon can be used as a measure of temperature. This is strongly temperature dependent (approximately proportional to  $T^{-1.8}$ ) and well defined for the highly pure silicon used in ICs [10]. A TD-based temperature sensor (TD sensor) operates by measuring the time that it takes for heat pulses from a heater, usually a diffusion resistor, to diffuse through the substrate to a relative temperature sensor, usually a thermopile. This diffusion process can be modeled as an electro-thermal low-pass filter, whose delay is in the order of a few micro-seconds for heater/thermopile spacings of a few micrometers. The corresponding phase shift is approximately proportional to absolute temperature ( $\sim T^{0.9}$ ) [10].

The accuracy of an electrothermal filter (ETF) is mainly limited by variations in the spacing between the heater and the thermopile, which, in turn, is determined by the lithographic accuracy of the process used. Thus, the accuracy of TD sensors actually improves with technology scaling, as does the timing accuracy of their readout circuitry [11]. Moreover, since the required heat pulses can be generated from any supply voltage, TD sensors can be easily ported to newer technologies with lower supply voltages.

It has been shown that TD sensors can achieve untrimmed inaccuracy below 0.2 °C in 0.18- $\mu\text{m}$  CMOS [11]. However, the reported smart sensor was too large (0.18 mm<sup>2</sup>) and too slow (1 Sa/s) for thermal monitoring applications. By employing more compact electronics, much

smaller smart TD sensors with areas of  $8000 \mu\text{m}^2$  [12], and even  $2800 \mu\text{m}^2$  [13], have been reported. However, these sensors were also implemented in a relatively mature  $0.16\text{-}\mu\text{m}$  CMOS process.

This work presents the first TD sensor realized in nanometer ( $40 \text{ nm}$ ) CMOS. It demonstrates that the performance of TD sensors indeed continues to improve with scaling. Without temperature calibration, the sensor achieves  $\pm 1.4^\circ\text{C}$  ( $3\sigma$ ) inaccuracy from  $-40^\circ\text{C}$  to  $125^\circ\text{C}$ , which is 5x better than previous (non-TD) sensors intended for thermal monitoring [4,14-16]. This improves to  $\pm 0.75^\circ\text{C}$  ( $3\sigma$ ) after a single-temperature calibration, a level of accuracy that, for non-TD sensors, requires two-temperature calibration [4,14,15]. Furthermore, it operates from a  $0.9\text{-V}$  supply, and occupies only  $1650 \mu\text{m}^2$ , making it one of the smallest smart temperature sensors reported to date.

This paper begins with a description of the ETF design in section II and continues with the system level design in section III. The circuit implementation is detailed in section IV. Experimental results are shown in section V and conclusions are drawn in section VI.

## II. ELECTRO-THERMAL FILTER DESIGN

The simplified layout of an ETF realized in a standard  $40\text{-nm}$  CMOS process is shown in Fig. 1. The heater is a diffusion resistor, while the relative temperature sensor is a thermopile, i.e. a series connection of p+ silicon/Aluminum thermocouples. The heater is driven by a square wave at a constant frequency, so that the ETF's temperature-dependent delay manifests itself as a phase-shift in the thermopile's output voltage. **The whole structure is placed in an n-well to shield it from electrical interference via the substrate. The effect of thermal interference via the substrate (e.g. due to other on chip circuitry) is not a concern, since this will be strongly low-pass filtered in the thermal domain [16].**

In Fig. 1, the hot junction of each thermocouple, i.e. the p+/Al contact closest to the heater, is located at a distance  $s$  from the ETF's center, while the cold junctions are further away. Since each thermocouple produces a voltage proportional to the temperature difference between its hot and cold junctions, the ETF's output signal is larger for a shorter  $s$  and for longer thermocouple arms. However, reducing  $s$  means a larger sensitivity to lithographic errors, thus resulting in lower accuracy, while longer thermocouple arms have higher resistance, thus causing higher thermal noise.

Previous ETFs were optimized for accuracy at the expense of signal-to-noise ratio (SNR), which meant that their heater/thermopile spacing was relatively large ( $s = 24 \mu\text{m}$ ). As a result, their readout bandwidth had to be less than 1 Hz to achieve reasonable resolution [17]. In this work, we leverage the improved lithographic accuracy of nanometer CMOS to implement ETFs with much smaller heater/thermopile spacing in order to improve SNR without significantly degrading accuracy. Moreover, an octagonal layout is used that minimizes thermopile resistance, and hence thermal noise, by maximizing the thermopile width. In this work, two ETFs were realized, with  $s = 3.3 \mu\text{m}$  and  $2 \mu\text{m}$ , respectively, in order to explore the influence of  $s$  on ETF performance. Both ETFs occupy an area of  $240 \mu\text{m}^2$  and dissipate an average power of 2.1 mW from a 1.05-V supply.

For compatibility with previous work [12], the ETF drive frequency ( $F_{\text{DRIVE}}$ ) is set at 1.17 MHz. From -40 to 125 °C, the phase shifts of the  $s = 3.3 \mu\text{m}$  and  $2 \mu\text{m}$  ETFs are then expected to range from 35° to 60°, and from 25° to 45°, respectively. Based on thermal modeling, the corresponding output levels are expected to be 1.3 mVpp and 2.4 mVpp, respectively, for a heater power dissipation of 1mW [18]. Combined with the parasitic capacitance of the thermopiles, the thermopile's resistance  $R_{\text{TP}}$ , about 8 kΩ and 12 kΩ for the 3.3-μm and 2-μm ETFs, respectively, causes an additional phase shift of 0.4° and 0.6°. The spread on this RC

phase shift (about 30% over corners) will give rise to an equivalent temperature-sensing spread of less than 0.9 °C.

### III. SYSTEM LEVEL DESIGN

The target sampling rate of 1 kSa/s and the small area requirement pose significant challenges on the design of the readout architecture. Fundamentally, an ETF's temperature information is contained in the phase delay of a small (~mV amplitude) signal, and so a sensitive and high-resolution phase-domain ADC is necessary. As shown in previous work [11,17], the phase-domain  $\Sigma\Delta$  modulator (PDE $\Sigma\Delta$ M) is a good candidate for this purpose. A PDE $\Sigma\Delta$ M is a  $\Sigma\Delta$  modulator with a feedback path in the phase domain. The required phase-domain summation node can be realized by a chopper demodulator, which demodulates the phase of the ETF signal (at a frequency  $F_{\text{DRIVE}}$ ) by multiplying it with a square-wave at  $F_{\text{DRIVE}}$ , but with a known (reference) phase shift [17]. **A PDE $\Sigma\Delta$ M thus incorporates a synchronous phase detector and as such is only sensitive to interferers at frequencies very close to the drive frequency  $F_{\text{DRIVE}}$ . In an SoC, the presence of such interferers can readily be avoided by proper frequency planning.**

Fig. 2 shows the block diagram of a first-order PDE $\Sigma\Delta$ M. A gm-stage converts the ETF's output voltage (at frequency  $F_{\text{DRIVE}}$ ) into current, whose phase shift ( $\Phi_{\text{ETF}}$ , measured with respect to the phase of the signal driving the ETF's heater) is detected by a chopper demodulator driven by  $F_{\text{DEM}}$ . The phase-dependent DC current is then integrated on a capacitor and applied to a latched comparator, whose bitstream output (BS) switches  $F_{\text{DEM}}$  between outputs of a phase DAC ( $\Phi_{\text{DAC}}$ ) in a  $\Sigma\Delta$  manner. For a single-bit modulator,  $\Phi_{\text{DAC}}$  switches between the two phase references,  $\Phi_0$  and  $\Phi_1$ .  $F_{\text{DRIVE}}$  and phase DAC outputs can be generated by a digital block, which is driven by an accurate high frequency clock ( $F_{\text{SYNC}}$ ) [12]. However, such PDE $\Sigma\Delta$ Ms require large integration capacitors and high-gain amplifiers [12], which in turn occupy significant area. Moreover, because of the need for high-gain amplifiers, this architecture does not scale well with technology [19].

A more digital-friendly architecture was proposed in [20] and is shown in Fig. 3. In such VCO-based PD $\Sigma$ AM, the combination of a voltage-controlled oscillator (VCO) and an up/down counter replaces the gm-stage, the chopper and the integration capacitor. Here, the ETF output signal  $V_{ETF}$  at frequency  $F_{DRIVE}$  and phase shift  $\Phi_{ETF}$  modulates the VCO's output frequency ( $F_{VCO}$ ). An all-digital  $\Delta\Sigma$  modulator then synchronously demodulates the VCO's output and digitizes the ETF's phase shift  $\Phi_{ETF}$ . The functions of demodulation and integration are realized by the up/down counter, whose  $M$  most-significant bits (MSB) of its output word constitute the output bitstream. Such bitstream drives the phase DAC, which applies a digitally-delayed feedback signal ( $F_{DEM}$ ) to the counter's up/down input. To improve accuracy, the modulator is usually operated as an incremental converter, where the counter is reset before each conversion [21]. The decimation filter can then be a simple counter (sinc filter) [20]. In contrast to previous work, a multi-bit DAC ( $M = 3$ ) is chosen in this work, a choice which reduces both quantization noise and the inherent cosine non-linearity of synchronous phase demodulation [11] to negligible levels ( $\pm 0.04$  °C). This avoids the complexity of a two-step conversion with single-bit incremental converters [12], without compromising performance.

However, a disadvantage of the proposed architecture is that the finite bandwidth of the VCO in Fig. 3 results in additional phase shift, which cannot be distinguished from  $\Phi_{ETF}$ . In fact, while the gm-stage in Fig. 2 can be implemented by a fast differential pair immediately followed by a demodulating analog chopper [17], the VCO in Fig. 3 requires both a low-noise front-end and a cascaded oscillator element, and thus is inherently slower. In this work, the VCO's phase error is mitigated by a phase-calibration scheme in which the entire VCO-based PD $\Sigma$ AM is driven by a reference square-wave ( $V_{CAL}$ ) with a known phase shift ( $\Phi_{CAL}$ ). The additional phase error introduced by the readout can thus be determined and then subtracted from the results of subsequent conversions.



Fig. 4 shows the block diagram of a VCO-based PDΣΔM with phase calibration. Here, the VCO front-end is implemented as a gm stage followed by a current-controlled oscillator (CCO). The gm-stage isolates the weak  $\sim mV_{pp}$  ETF signal from the CCO to prevent kick-back and also acts as a low-noise amplifier. The CCO drives an 8-bit up-down counter, whose 3 MSBs are latched by D flip-flops to realize the quantizer of a 3-bit ΣΔ modulator. The 3-bit unary phase DAC consists of a 3-bit multiplexer selecting the outputs of an 8-element delay line that shifts an input signal ( $F_{DL}$ ), where  $\angle F_{DL} = \angle F_{DRIVE} + 90^\circ$ . The reference delay signal ( $F_{SYNC}$ ) is an external 75-MHz clock, while  $F_{DRIVE} = 1.17$  MHz. This results in a phase DAC LSB of  $5.625^\circ$ , but in order to cover a large range, the DAC LSB was chosen to be  $11.25^\circ$  in practice via dividing  $F_{SYNC}$  by 2. Therefore, the DAC spans from  $101.25^\circ$  to  $180^\circ$ . In order to minimize any circuit related delay, and hence any additional phase error in  $F_{DRIVE}$  and  $F_{DEM}$ , both clock signals are synchronized by  $F_{SYNC}$  before being delivered to the heater switches or to the up/down counter. Unlike prior work employing analog choppers [12], low-frequency chopping is not necessary to eliminate the residual offset due to chopper non-idealities because the up/down counter behaves like a near-ideal digital chopper. This further simplifies the drive logic, thus saving additional area.

The phase-calibration reference signal is generated by injecting a reference current from a current source ( $I_{CAL}$ ) into the thermopile's resistances  $R_{TP}$ . The reference phase for phase calibration was chosen equal to  $22.5^\circ$ , a phase which requires only two flip-flops to generate.

The total budget for thermal noise (resolution), electrical phase delay (accuracy) and power of the proposed TD sensor is shown in Table I. The gm stage is optimized for low-power consumption and low area, thus leading to a gm-stage design that contributes  $\sim 30\%$  of the total thermal noise and about half of the phase delay budgets.

In addition to thermal noise, the PDΣΔM's resolution is also affected by the quantization noise imposed by the CCO and counter combination. This occurs because the counter only

recognizes the rising edges of  $F_{VCO}$ , effectively quantizing the time-domain information coming from the CCO. In most amplitude-domain VCO-based ADCs, the VCO is cascaded to a fully-analog loop filter, thus providing high-pass shaping of this noise and effectively removing it from the band of interest [22]. Unfortunately, this is not the case for a phase-domain modulator. Indeed, CppSim [23] simulations of the PDS $\Delta$ M shown in Fig. 4 reveal that this quantization noise manifests itself as an input-referred white noise source. Nevertheless, simulations also confirm intuition in showing that such time-domain quantization noise is lower for a higher  $F_{VCO}$  frequency. For the proposed design, the nominal VCO frequency ( $F_{NOM}$ ) is 630 MHz, while the voltage-to-frequency gain of the VCO ( $K_{VCO}$ ) is 200 MHz/mV. With these values, simulations show that the additional quantization noise due to VCO is about 25 m $^{\circ}$  in a 500-Hz bandwidth, which translates into a temperature-sensing resolution of 0.16  $^{\circ}$ C.

#### IV. CIRCUIT DESCRIPTION

Fig. 5 shows the circuit level implementation of the gm-stage that supplies the CCO. The CCO can be modeled as a non-linear impedance  $r_{CCO}$  sinking a current  $I_{CCO}$ . For maximum efficiency and driving capability,  $r_{CCO} \ll r_o$ , where  $r_o$  is the output impedance of the gm stage. Although  $r_{CCO}$  depends on the CCO architecture, it is typically in the order of tens of k $\Omega$ 's. Therefore, the gm stage requires a high output impedance, as well as a high transconductance (gm) to meet the noise requirements shown in Table I. Moreover, it needs to work a supply voltage below 1 V to demonstrate compliance with current and future supply voltages for nanometer CMOS (1.1 V for 40-nm CMOS). In 40-nm CMOS technology, these three requirements necessitate the use of a two-stage amplifier architecture. A two-stage design also uses less transistors (8) than a folded-cascode (11) amplifier [17], and thus occupies less area. Although a two-stage amplifier may have larger delay than a single-stage amplifier, this can be compensated by the phase calibration.

The first stage (M1-4) is optimized for minimal thermal noise, and phase shift at  $F_{\text{DRIVE}}$  and has a gain of 25 dB and a bandwidth of 300 MHz. Its 10-nV/ $\sqrt{\text{Hz}}$  noise density (see Table I) is mostly dominated by the input pair M1-2. The second stage (M5) adds gain for an overall gm of 2.5 mA/V. It is cascoded by M6 to boost its output impedance  $r_O$  from  $\sim 80 \text{ k}\Omega$  to  $\sim 400 \text{ k}\Omega$  without significantly compromising CCO's voltage headroom. With this configuration, the circuit operates correctly with a supply voltage as low as  $2V_{\text{GS}} + 2V_{\text{DS}} \cong 0.8 \text{ V}$  ( $2V_{\text{GS}}$  for the CCO headroom and  $2V_{\text{DS}}$  for M5 and M6 in Fig. 5).

The offset of the gm-stage together with the PVT variations of the CCO can create a large spread in the nominal CCO frequency  $F_{\text{NOM}}$ . An excessively high  $F_{\text{NOM}}$  can cause counter failure while an excessively low  $F_{\text{NOM}}$  can both cause excessive quantization noise and force the CCO in a highly non-linear operating region. Moreover, large changes of  $F_{\text{NOM}}$  over temperature can cause the delay of the VCO to change, and add a temperature-dependent phase error, i.e. more inaccuracy. Therefore,  $F_{\text{NOM}}$  is trimmed by a 6-bit current DAC (IDAC) before every conversion. During this process, the counter is configured to only count up, while external logic implements a simple ramp algorithm that monitors the counter's 4th LSB (toggling at  $F_{\text{VCO}}/16$ ) and increments the IDAC's input until  $F_{\text{VCO}}$  is  $\sim 630 \text{ MHz}$ . This whole calibration process takes less than 100  $\mu\text{s}$  over the specified supply-voltage and temperature range. One LSB of the trimming IDAC corresponds to a 62.5-MHz average step on  $F_{\text{NOM}}$ , thus resulting in  $F_{\text{NOM}} = 630 \text{ MHz} \pm 62.5 \text{ MHz}$ , which is enough to guarantee negligible phase error. The IDAC can compensate an error up to  $\pm 20 \text{ mV}$  referred at the gm-stage input, which is large enough to cover PVT variations as well as amplifier offset.

During phase calibration, the current source for phase calibration (ICAL in Fig. 4) is switched between the two thermopile resistors of the ETF to generate an AC square wave with amplitude up to 2 mV<sub>pp</sub> at the gm input. Biasing transistor M7 determines the common mode voltage of the ETF thermopiles. ICAL has been designed as a 2-bit current DAC with a unit current of 125

nA, in order to test the effect of front-end non-linearity on the phase-calibration technique. Since this non-linearity was found to be negligible during experimental characterization, ICAL is always operated at its maximum current of 500 nA.

Fig. 6 shows the circuit level implementation of CCO. The gm-stage is modelled as a current source  $I_{CCO}$  with impedance source resistance of  $r_O$ . In order to minimize area and maximize CCO gain ( $K_{CCO}$ ), the CCO is implemented as a ring oscillator with the minimum number of stages, i.e. 3 stages. Each transistor in the inverters is sized with minimum length and twice the minimum width, to ensure that CCO output swing is low enough to ensure voltage headroom at the output of the gm state for sub-1V operation. With these design choices,  $r_{CCO}$  is  $\sim 30\text{ K}\Omega$  at 25 °C and is much smaller than  $r_O$ , as intended.

The impact of the CCO's phase noise on the sensor's resolution is reduced by the gain of the preceding gm-stage. Moreover, only a narrow-band component of this noise around  $F_{DRIVE}$  is involved, since the CCO's output is synchronously demodulated. As a result, the noise of the gm-stage is dominant in this design. As explained before, the CCO's PVT variation is corrected by trimming  $F_{NOM}$  before every conversion.

Since the CCO's voltage swing is small and depends on PVT, it is boosted to logic-compatible levels by a single-stage differential amplifier (M1-4) referenced to a replica inverter. The amplifier is designed for speed, since its delay adds to the phase shift of the gm-stage. It has a nominal AC gain of 10 dB over a bandwidth of 900 MHz and consumes only 50  $\mu\text{A}$ . After the amplifier, three tapered inverters provide the strength to drive the 8-bit counter.

The 8-bit up/down counter was synthesized from standard cells and laid out via a standard place-&-route tool. According to simulation, it can operate at a clock frequency up to 1 GHz over all corners, 0.9-1.2V supply voltage and the temperature range. The up/down signal ( $F_{DEM}$ ) is re-clocked by  $F_{VCO}$  to avoid metastability in the counter. The 3-bit sampling register also

employs standard cells and its sampling clock ( $F_S$ ) is generated by the digital logic and is re-clocked by the falling edge of  $F_{VCO}$ , which means that the up/down counter must settle within a half period of  $F_{VCO}$ .

Fig. 7 shows the schematic of the digital logic that generate the signals driving the ETF heater and the counter, along with the truth table describing the function of the combinational logic. The heater-driving transistor MD controls the current flow in the ETF heater  $R_{HEAT}$  to create the ETF heat pulse. To minimize the parasitic series resistance and hence maximize the power efficiency of the ETF, each heater ( $R_{HEAT} = 188 \Omega$ ) is driven by a large NMOS ( $W=68 \mu\text{m}$ ,  $L=40 \text{ nm}$ ,  $R_{on} \sim 20 \Omega$ ). The large gate capacitance of MD is driven by a digital buffer implemented as tapered inverters. Since any delay mismatch between  $F_{DRIVE}$  and  $F_{DEM}$  would result in a phase error and, consequently, in additional inaccuracy, the up/down signal path mirrors the drive path by using the same synchronizing flip-flop and digital buffer between the phase DAC output ( $F_{DAC}$ ) and the counter input ( $F_{DEM}$ ).

The signals CAL\_MODE and TRIM set the system in phase calibration and CCO trimming modes, respectively. When either mode is selected, a relatively high frequency signal ( $F_{SYNC}/2$ ) is provided to the ETF. At this frequency, the ETF's AC output is quite small, while the same self-heating-induced DC offset is present as in normal operation [11]. In addition, when phase calibration is enabled, a delayed version of  $F_{DRIVE}$  (generated by an auxiliary output of the phase DAC) is delivered to the gm-stage via  $F_{CAL}$ . When TRIM mode is enabled, the counter is forced to count only up and both the ETF input and the  $F_{CAL}$  signals are disabled to guarantee that the VCO only sees the offset of the gm-stage and the self-heating of the ETF.

## V. EXPERIMENTAL RESULTS

The prototype was realized in a standard 40-nm CMOS process and occupies an active area of  $0.23 \text{ mm}^2$  (Fig. 8). It consists of an array of 12x2 sensors, 12x2 test structures, 2 test heaters

(resistors), a shared bias-current generator and shared digital I/O logic (shift registers and multiplexers for testability). Each sensor occupies  $61\ \mu\text{m} \times 27\ \mu\text{m}$ , and dissipates 2.5 mW, most of which (88%) is dissipated in the ETF.

In each sensor, the ETF occupies only 15% of the  $1650\ \mu\text{m}^2$  sensor area, while the analog and digital circuitry occupy 25% and 60%, respectively. In 40-nm CMOS, the sensor is about 2x smaller than previous designs in 160-nm CMOS [13], even though it includes many additional features, such as phase calibration, multi-bit feedback and the phase DAC's reference generation. The area required for the decimation filter and the CCO's trimming logic is estimated to be about  $600\ \mu\text{m}^2$ , but since those functions do not necessarily need to be co-located within the sensor, they were implemented off-chip for flexibility. Functionality of each sensor was verified over (digital and analog) supply voltages ranging from 0.9 to 1.2 V (nominal supply is 1.05V), and a  $2.8\ \text{°C/V}$  supply sensitivity was observed over such range.

The phase vs. temperature characteristics of both ETFs from  $-40$  to  $125\ \text{°C}$  (averaged over 24 dies and 144 sensors for each ETF) at 1.17-MHz drive frequency were used to generate the 5<sup>th</sup>-order polynomial master curves shown in Fig. 9. Those master curves were used to convert the decimated output of each PDSΔM into a temperature reading. Over the measured temperature range, the master curves can be well approximated by a  $T^n$  power-law [23]. For the 3.3- $\mu\text{m}$  and 2- $\mu\text{m}$  ETFs, good fits were obtained with  $n=0.98$  and  $n=0.95$ , respectively, which agrees well with previous work [12,24].

Fig. 10 shows the power spectral density (PSD) of the 3-bit digital output of both the 3.3- $\mu\text{m}$  and 2- $\mu\text{m}$  ETF's. The thermal noise floor corresponds to a resolution of 0.36  $\text{°C}$  (RMS) for the 3.3- $\mu\text{m}$  ETF and 0.24  $\text{°C}$  (RMS) for the 2- $\mu\text{m}$  ETF, both obtained for a bandwidth of 500 Hz, i.e. at a sampling rate of 1 kSa/s.

The additional phase due to the readout can be detected and removed via phase calibration. Fig. 11 shows the phase error of the readout circuitry of 144 sensors, measured at a reference phase of  $22.5^\circ$  (Fig. 11). The mean phase error is  $1.3^\circ$  and it exhibits a slight curvature over temperature. Phase calibration can be done continuously, e.g. after every conversion, but at the expense of halving the conversion rate and degrading the resolution from  $0.24^\circ\text{C}$  for the  $2\text{-}\mu\text{m}$  ETF ( $0.36^\circ\text{C}$  for the  $3.3\text{-}\mu\text{m}$  ETF) to  $0.40^\circ\text{C}$  ( $0.5^\circ\text{C}$ ). Alternatively, it can be done one-time at room temperature after fabrication but at the expense of increased inaccuracy.

As shown in Fig. 12, the sensors based on the  $3.3\text{-}\mu\text{m}$  ETF achieve an untrimmed inaccuracy of  $\pm 1.8^\circ\text{C}$  ( $3\sigma$ , 144 sensors, 24 dies) from  $-40$  to  $125^\circ\text{C}$  for a supply voltage of  $1.05\text{V}$ . The inaccuracy improves to  $\pm 1.4^\circ\text{C}$  ( $3\sigma$ ) after a one-time phase calibration at room temperature, and to  $\pm 0.75^\circ\text{C}$  ( $3\sigma$ ) after temperature calibration at  $25^\circ\text{C}$ . Continuous phase calibration improves inaccuracy to  $\pm 0.5^\circ\text{C}$  ( $3\sigma$ ). At a  $0.9\text{-V}$  supply voltage, the digital logic slows down, resulting in an untrimmed inaccuracy of  $\pm 2.3^\circ\text{C}$  ( $3\sigma$ ), and  $\pm 1.2^\circ\text{C}$  ( $3\sigma$ ) after trimming.

The improved resolution of the  $2\text{-}\mu\text{m}$  ETFs comes at the expense of accuracy, as shown in Fig. 12. Their untrimmed inaccuracy is  $\pm 2.3^\circ\text{C}$  ( $3\sigma$ , 144 sensors, 24 dies) after a one-time or continuous phase calibration. After a single-temperature calibration, those values reduce to  $\pm 1.05^\circ\text{C}$  ( $3\sigma$ ) and  $\pm 0.85^\circ\text{C}$  ( $3\sigma$ ), respectively.

Self-heating of the ETFs ( $1.7^\circ\text{C}$  and  $4^\circ\text{C}$  for the  $3.3\text{-}\mu\text{m}$  and  $2\text{-}\mu\text{m}$  ETF, respectively) is estimated to spread by approximately 20% due to the spread in heater resistance and in parasitic resistance of the driving transistor. This results in an error of  $\pm 0.35^\circ\text{C}$  ( $3\sigma$ ) for the  $3.3\text{-}\mu\text{m}$  ETF and  $\pm 0.8^\circ\text{C}$  ( $3\sigma$ ) for the  $2\text{-}\mu\text{m}$  ETF, which is already included in the  $\pm 1.4^\circ\text{C}$  ( $3.3\text{-}\mu\text{m}$  ETF) and  $\pm 2.3^\circ\text{C}$  ( $2\text{-}\mu\text{m}$  ETF) values reported above.

In order to test the sensor's sensitivity to mechanical stress, 16 dies (each containing  $6 \times 3.3\text{-}\mu\text{m}$  ETF and  $6 \times 2\text{-}\mu\text{m}$  ETFs) were packaged in standard SO28 plastic packages. As shown in

Fig. 13, the untrimmed inaccuracy of 96, 3.3- $\mu\text{m}$  ETFs, was  $\pm 2.3$   $^{\circ}\text{C}$  ( $3\sigma$ ). Compared to the ceramic-packaged devices, more spread was observed, which may be due to the additional self-heating in plastic packages and to the stress sensitivity of the thermal diffusivity of silicon [25]. After a PTAT trim, the spread drops to  $\pm 0.75$   $^{\circ}\text{C}$  ( $3\sigma$ ); which is the same for plastic and ceramic packaged sensors.

To characterize the nonlinearity of the PD $\Sigma$  $\Delta$ M, they were exposed to a temperature ramp from -40 to 125  $^{\circ}\text{C}$ . Fig. 14 shows the statistical averages obtained from a 50 mK/sample ramp. It can be seen that no artifacts occur during the measurement.

The sensor's performance with both ETFs is summarized in Table II and compared to that of other sensors intended for thermal-monitoring applications. Due to the amount of power dissipated in the ETF, the proposed sensor is not particularly energy efficient, as can be seen from its relatively poor resolution FoM [28]. However, with the 3.3- $\mu\text{m}$  ETF, the proposed sensor is the most accurate and the smallest, except for a sensor that requires an accurate external voltage reference (which is not included in the reported area) [15]. It also has the second lowest operating supply voltage (0.9 V), which is mainly limited by the up/down counter. Compared to TD sensors implemented in more mature technologies [13], it achieves 1.5x better resolution and 2x more accuracy, while requiring about 2x less area.

## VI. CONCLUSIONS

A compact TD sensor in 40-nm CMOS has been described, and techniques which allow the sensor to be implemented in a compact area have been presented. The sensor's area, speed, resolution and power-supply rejection satisfy typical specifications for SoC thermal monitoring, while its untrimmed inaccuracy is the lowest reported for temperature sensors in nanometer CMOS below 40 nm. The performance (area, accuracy, power, speed) of TD sensors has been demonstrated to improve with process scaling, and additional improvements can be reasonably expected in future more advanced technologies. These results demonstrate that TD-based



temperature sensors are suitable for hot-spot monitoring in microprocessors and other systems-on-chip.

## REFERENCES

- [1] E. Rotem, J. Hermerding, C. Aviad, and C. Harel, "Temperature measurement in the Intel Core Duo processor," *Proc. THERMINIC*, pp.23–27, Sep. 2006.
- [2] J. Shor, and K. Luria, "Miniaturized BJT-based thermal sensor for microprocessors in 32- and 22-nm Technologies," *IEEE Journal of Solid-State Circuits*, vol.48, no.11, pp.2860-2867, Nov. 2013.
- [3] M. Floyd, et al., "Introducing the adaptive energy management features of the Power7 chip," *IEEE Micro*, vol.31, no.2, pp.60-75, Mar.-Apr. 2011.
- [4] H. Lakdawala et al., "A 1.05V 1.6mW 0.45°C 3 $\sigma$ -resolution  $\Delta\Sigma$ -based temperature sensor with parasitic-resistance compensation in 32 nm digital CMOS process," *IEEE Journal of Solid-State Circuits*, vol.44, no.12, pp.3621-3630, Dec. 2009.
- [5] T. Oshita, J. Shor, D. E. Duarte and A. Kornfeld, "Compact BJT-Based Thermal Sensor for Processor Applications in 14 nm tri-Gate CMOS Process," *IEEE Journal of Solid-State Circuits*, vol.50, no.3, pp.799-807, Mar. 2015.
- [6] F. Sebastiano et al., "A 1.2-V 10- $\mu$ W NPN-based temperature sensor in 65-nm CMOS with an inaccuracy of 0.2 °C (3 $\sigma$ ) from -70 °C to 125 °C," *IEEE Journal of Solid-State Circuits*, vol.45, no.12, pp.2591-2601, Dec. 2010.
- [7] J.J. Horng, et al., "A 0.7V resistive sensor with temperature/voltage detection function in 16nm FinFET technologies," *Dig. VLSI Symposium*, pp.1-2, Jun. 2014.
- [8] D. Ha et al., "Time-domain CMOS temperature sensors with dual delay-locked loops for microprocessor thermal monitoring," *Transactions on VLSI*, is. 9, pp. 1590-1601, Sep. 2012.
- [9] S. Hwang et al., "A 0.008 mm<sup>2</sup> 500  $\mu$ W 469 kS/s frequency-to-digital converter based CMOS temperature sensor with process variation compensation," *IEEE Transactions on Circuits and Systems I*, vol. 60, pp. 2241 - 2248, Sep. 2013.
- [10] K.A.A. Makinwa, and M. F. Snoeij, "A CMOS Temperature-to-Frequency Converter With an Inaccuracy of Less Than 0.5°C (3 $\sigma$ ) From - 40°C to 105°C," *IEEE Journal of Solid-State Circuits*, vol.41, no.12, pp.2992-2997, Dec. 2006
- [11] C.P.L. van Vroonhoven, D. d'Aquino, and K.A.A. Makinwa, "A thermal-diffusivity-based temperature sensor with an untrimmed inaccuracy of  $\pm 0.2$  °C (3 $\sigma$ ) from -55°C to 125°C," *Dig. ISSCC*, pp. 314-315, Feb. 2010.
- [12] U. Sonmez, R. Quan, F. Sebastiano, and K.A.A. Makinwa, "A 0.008-mm<sup>2</sup> Area-Optimized Thermal-Diffusivity-Based Temperature Sensor in 160nm CMOS for SoC Thermal Monitoring," *European Solid State Circuits Conference*, Sep. 2014.
- [13] J. Angevare et al., "A 2800- $\mu$ m<sup>2</sup> Thermal Diffusivity Temperature Sensor with VCO-Based Readout in 160-nm CMOS," *A-SSCC*, Nov. 2015.
- [14] T. Anand, K.A.A. Makinwa, and P. K. Hanumolu, "A Self-referenced VCO-based Temperature Sensor with 0.034°C/mV Supply Sensitivity in 65nm CMOS," *IEEE Journal of Solid-State Circuits*, vol. 51, issue 11, pp. 2651-2663, Sep. 2016.
- [15] G. Chowdhury and A. Hassibi, "An On-Chip Temperature Sensor With a Self-Discharging Diode in 32-nm SOI CMOS," *IEEE Trans. on Circuits and Systems II*, vol.59, no.9, pp.568-572, Sep. 2012.

- [16] C. P. L. van Vroonhoven and K. A. A. Makinwa, "A CMOS Temperature-to-Digital Converter with an Inaccuracy of  $\pm 0.5^\circ\text{C}$  ( $3\sigma$ ) from  $-55$  to  $125^\circ\text{C}$ ," *Dig. ISSCC*, pp. 576-637, Feb. 2008.
- [17] S.M. Kashmiri, S. Xia and K. Makinwa, "A Temperature-to-Digital Converter Based on an Optimized Electrothermal Filter," *IEEE Journal of Solid-State Circuits*, vol. 44, no. 7, pp. 2026-2035, July 2009.
- [18] T. Veijola, and M. Andersson, "Combined Electrical and Thermal Parameter Extraction for Transistor Model," *European Conference on Circuit Theory and Design*, pp. 754-759, Sep. 1997.
- [19] A. J. Annema, B. Nauta, R. van Langevelde and H. Tuinhout, "Analog circuits in ultra-deep-submicron CMOS," *IEEE Journal of Solid-State Circuits*, vol. 40, no. 1, pp. 132-143, Jan. 2005.
- [20] R. Quan, U. Sonmez, F. Sebastiano and K.A.A. Makinwa, "A  $4600\mu\text{m}^2$   $1.5^\circ\text{C}$  ( $3\sigma$ )  $0.9\text{kS/s}$  Thermal-Diffusivity Temperature Sensor with VCO-Based Readout," *Dig. ISSCC*, pp.488-489, Feb. 2015.
- [21] J. Robert et al., "A 16-bit low-voltage CMOS A/D converter," *IEEE Journal of Solid-State Circuits*, vol. 22, no.2, pp. 157-163, Apr. 1987.
- [22] M. Z. Straayer and M.H. Perrott, "A 12-Bit, 10 MHz Bandwidth Continuous Time  $\Sigma\Delta$  ADC with a 5-Bit  $950\text{ MS/s}$  VCO-Based Quantizer," *IEEE J. of Solid State Circuits*, vol. 43, no. 4, pp. 805-814, Apr. 2008
- [23] M.H. Perrott, "CppSim System Simulator Package," Online: <http://www.cppsim.com>
- [24] C. van Vroonhoven and K. Makinwa, "Thermal Diffusivity Sensors for Wide-Range Temperature Sensing," *IEEE Sensors*, pp. 764-767, Oct. 2008.
- [25] X. Li, K. Maute, M. L. Dunn and R. Yang, "Strain effects on the thermal conductivity of nanostructures," *Physical Review Letters B*, vol. 81, iss. 24, Jun. 2010.
- [26] M. C. Chuang et al., "A temperature sensor with a 3 sigma inaccuracy of  $\pm 2^\circ\text{C}$  without trimming from  $-50^\circ\text{C}$  to  $150^\circ\text{C}$  in a 16nm FinFET process," *European Solid-State Circuits Conference (ESSCIRC)*, pp. 271-274, Sep. 2015.
- [27] M. Eberlein and I. Yahav, "A 28nm CMOS ultra-compact thermal sensor in current-mode technique," *IEEE Symposium on VLSI Circuits (VLSI-Circuits)*, Jun. 2016.
- [28] K.A.A. Makinwa, "Smart Temperature Sensors in Standard CMOS," *Procedia Engineering*, pp. 930-939, Sep. 2010.

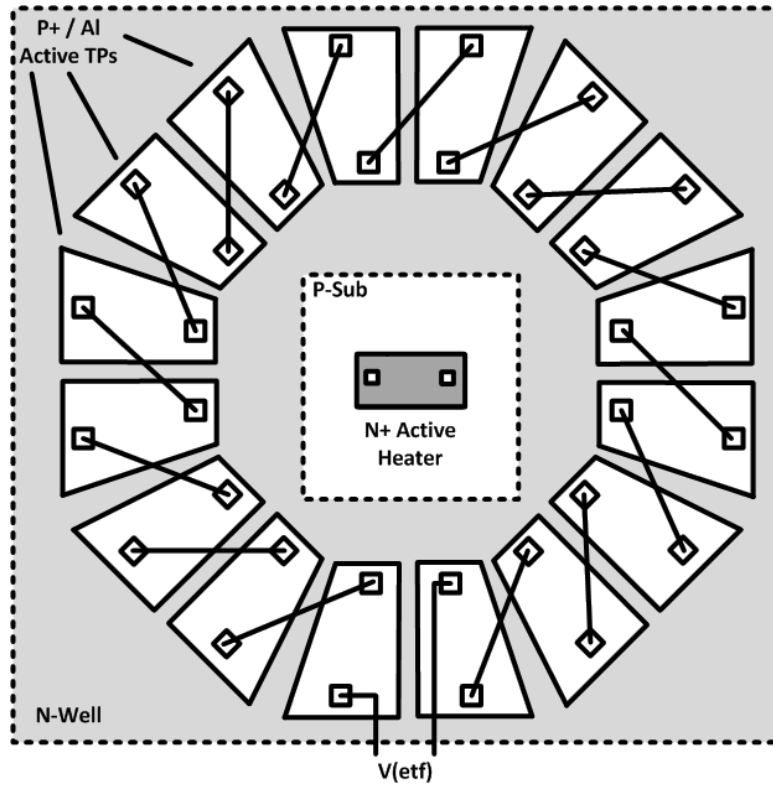


Fig. 1. Simplified layout of the proposed octagonal ETF in standard CMOS.

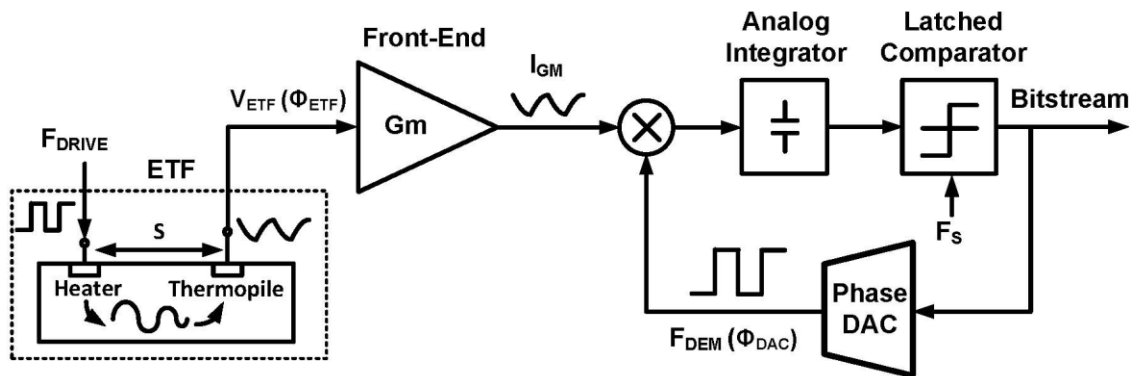


Fig. 2. Simple block diagram of a phase-domain  $\Sigma\Delta$  digitizing the phase output of an ETF.

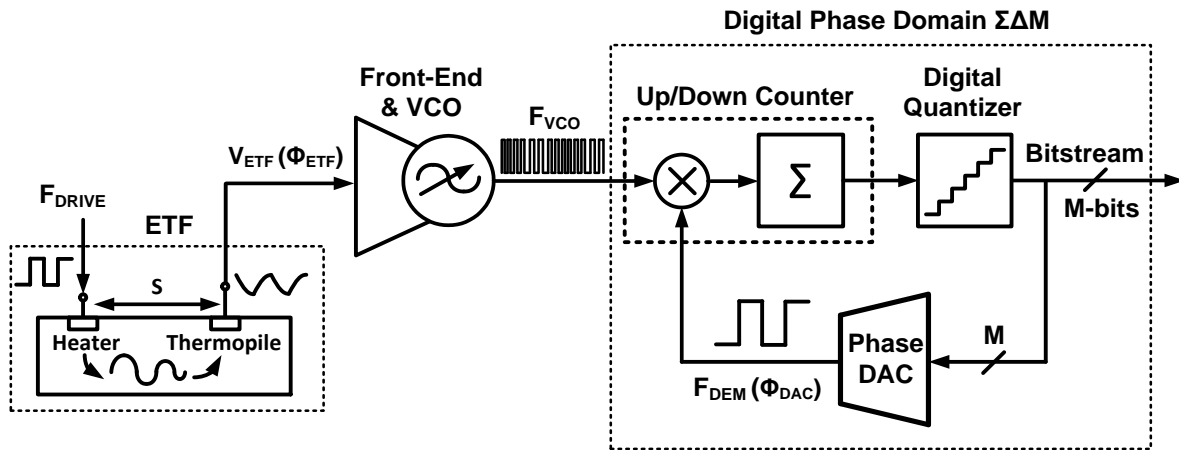


Fig. 3. Block diagram of a VCO-based phase-domain  $\Sigma\Delta$ .

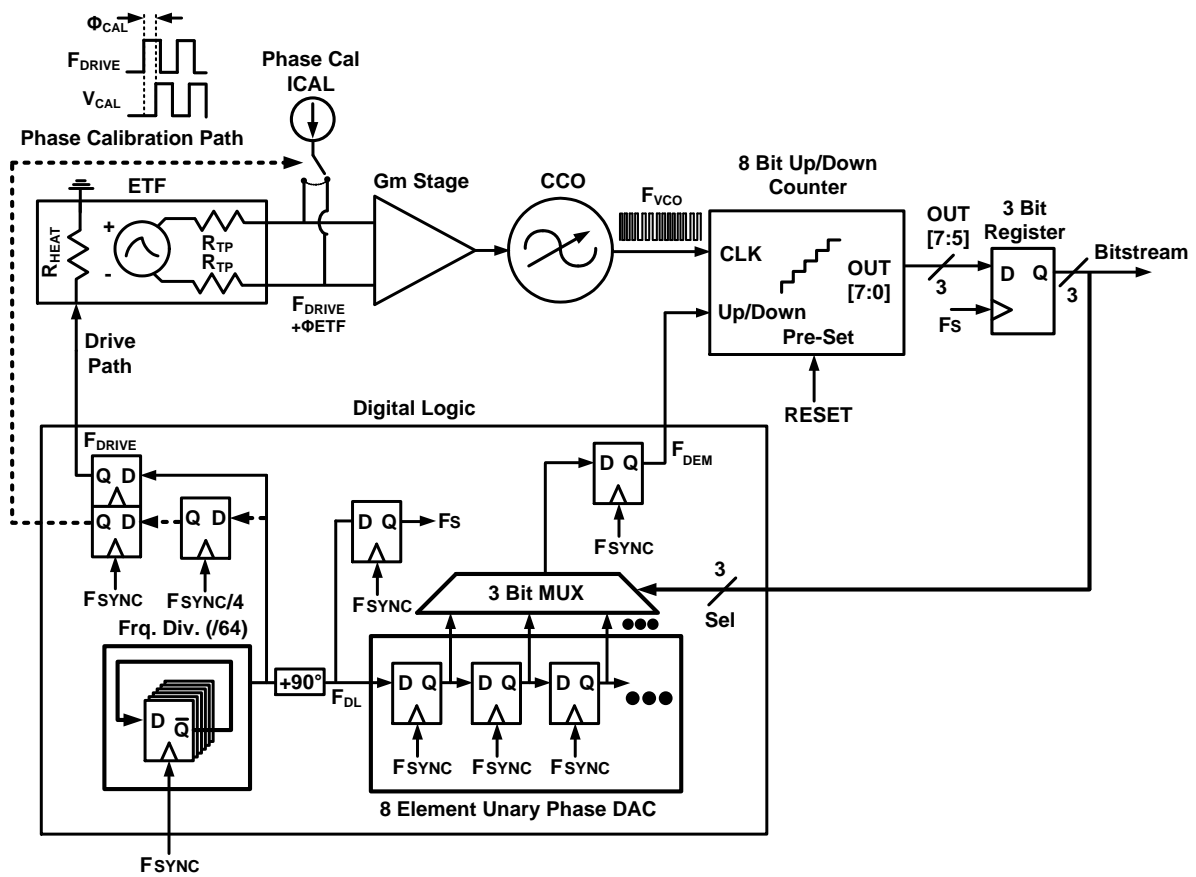


Fig. 4. Block diagram of the 3-bit VCO-based phase phase domain  $\Sigma\Delta$  modulator with phase calibration.

TABLE I. NOISE, DELAY AND POWER BUDGETING BETWEEN ETF AND READOUT BLOCKS

Circuit Block	Thermal Noise Density (Voltage)	Noise Density* (Phase)	Power**	Phase Delay ( $F_{DRIVE} = 1.17 \text{ MHz}$ )
ETF ( $s = 2 \text{ }\mu\text{m}$ )	13.7 nV/ $\sqrt{\text{Hz}}$	1.01 m $^\circ$ / $\sqrt{\text{Hz}}$	2.1 mW	0.6 $^\circ$
ETF ( $s = 3.3 \text{ }\mu\text{m}$ )	11.4 nV/ $\sqrt{\text{Hz}}$	1.54 m $^\circ$ / $\sqrt{\text{Hz}}$	2.1 mW	0.4 $^\circ$
<b>Gm-Stage + CCO</b> ( $s = 2 \text{ }\mu\text{m}$ )	10 nV/ $\sqrt{\text{Hz}}$	0.73 m $^\circ$ / $\sqrt{\text{Hz}}$	0.17 mW	0.75 $^\circ$
<b>Gm-Stage + CCO</b> ( $s = 3.3 \text{ }\mu\text{m}$ )		1.35 m $^\circ$ / $\sqrt{\text{Hz}}$		
Up/Down Counter	-	-	0.26 mW	-
Phase DAC	-	-	0.01 mW	0.1 $^\circ$
<b>Total (<math>s = 2 \text{ }\mu\text{m}</math>)</b>	17 nV/ $\sqrt{\text{Hz}}$	1.24 m $^\circ$ / $\sqrt{\text{Hz}}$	2.5 mW	1.45 $^\circ$
<b>Total (<math>s = 3.3 \text{ }\mu\text{m}</math>)</b>	15.2 nV/ $\sqrt{\text{Hz}}$	2.05 m $^\circ$ / $\sqrt{\text{Hz}}$	2.5 mW	1.25 $^\circ$

\* 1.3-mVpp ETF signal assumed for voltage to phase noise conversion for  $s = 3.3 \text{ }\mu\text{m}$   
 \* 2.4-mVpp ETF signal assumed for voltage to phase noise conversion for  $s = 2 \text{ }\mu\text{m}$   
 \*\*  $V_{DD} = 1.05 \text{ V}$

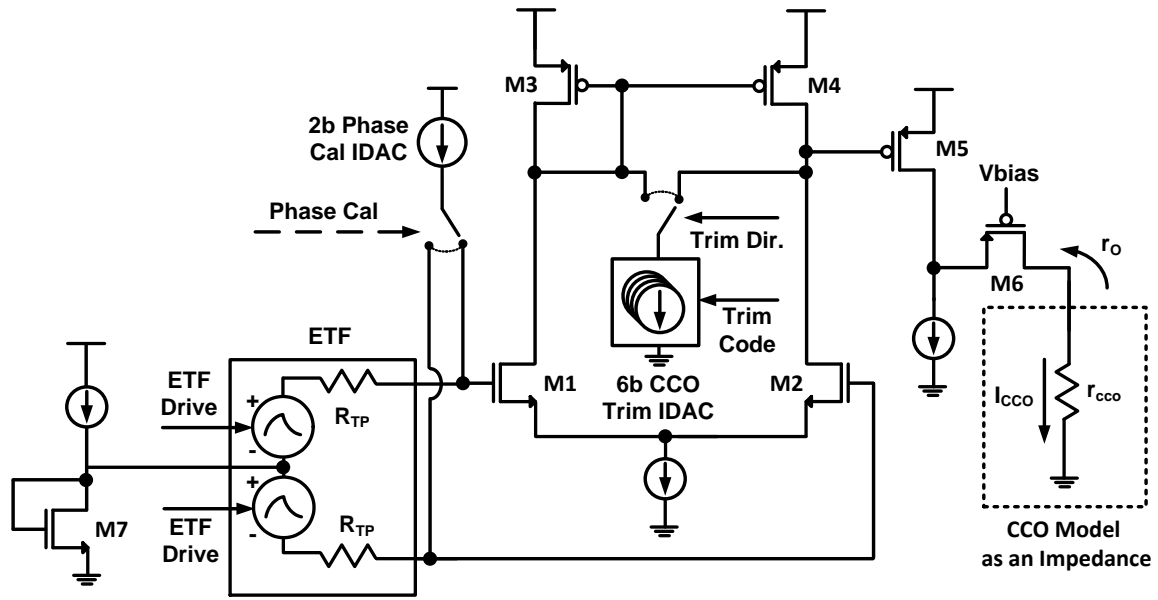


Fig. 5. Circuit diagram of the Gm-stage (cascaded CCO modelled as resistive load  $r_{CCO}$ )

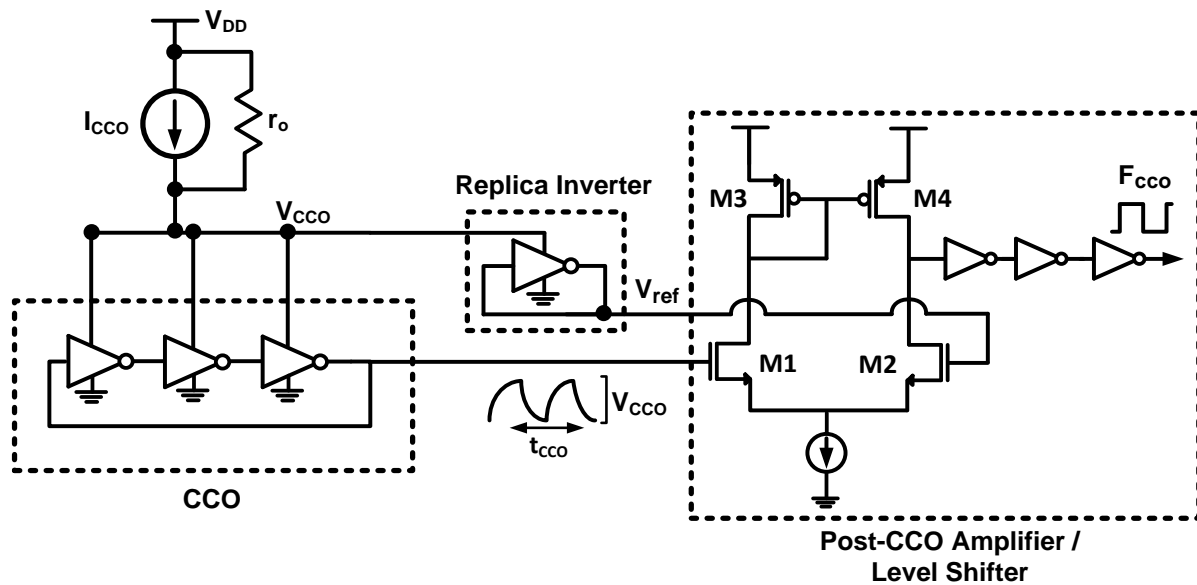
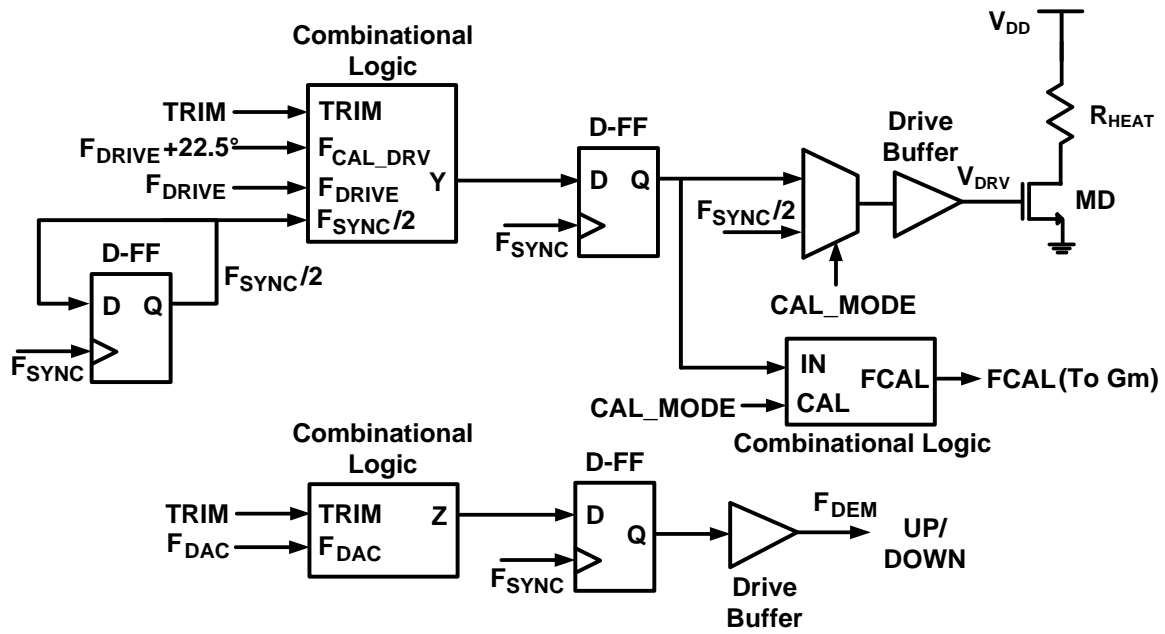


Fig. 6. Circuit diagram of the CCO and the cascaded level shifter amplifier. The driving gm stage is modelled with its Norton equivalent ( $I_{CCO}$  current source and  $r_o$  output impedance).



TRIM	CAL_MODE	Y	Z	FCAL	VDRV
0	0	$F_{DRIVE}$	$F_{DAC}$	0	$F_{DRIVE}$
0	1	$F_{CAL\_DRV}$	$F_{DAC}$	$F_{CAL\_DRV}$	$F_{SYNC}/2$
1	X	$F_{SYNC}/2$	0	0	$F_{SYNC}/2$

Fig. 7. Block diagram of the sensor digital logic for generation of  $F_{DRV}$  and  $F_{DEM}$  and truth table that describes the combinational logic function.

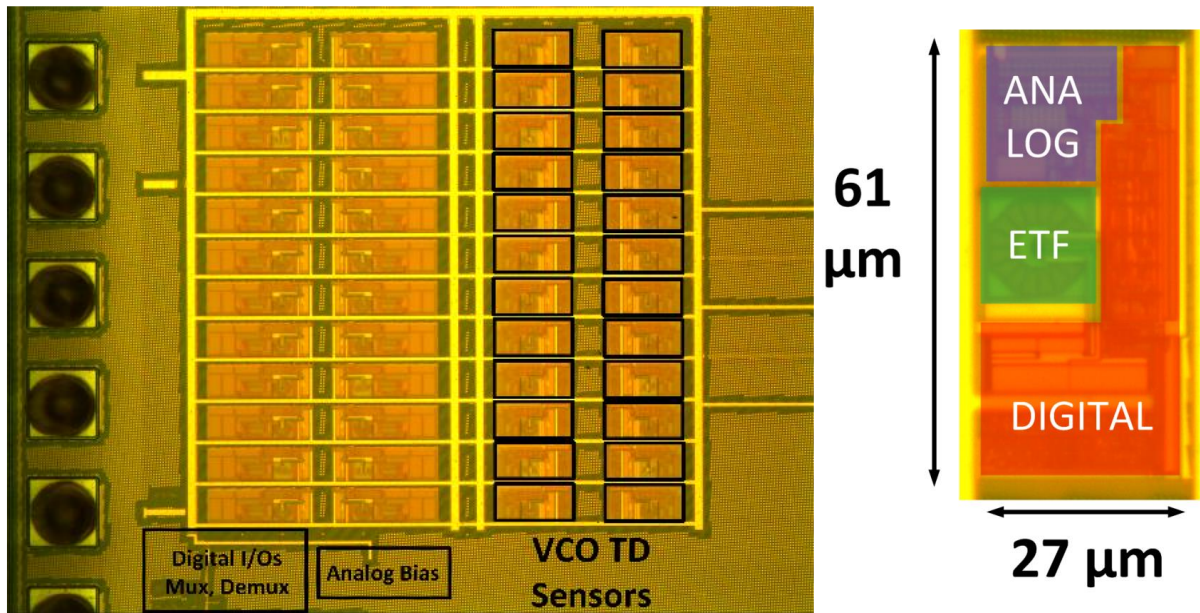


Fig. 8. Die photo, along with a zoomed-in photo of a single temperature sensor. The sensor's photo is showing the breakdown of area occupied by the ETF and circuitry.



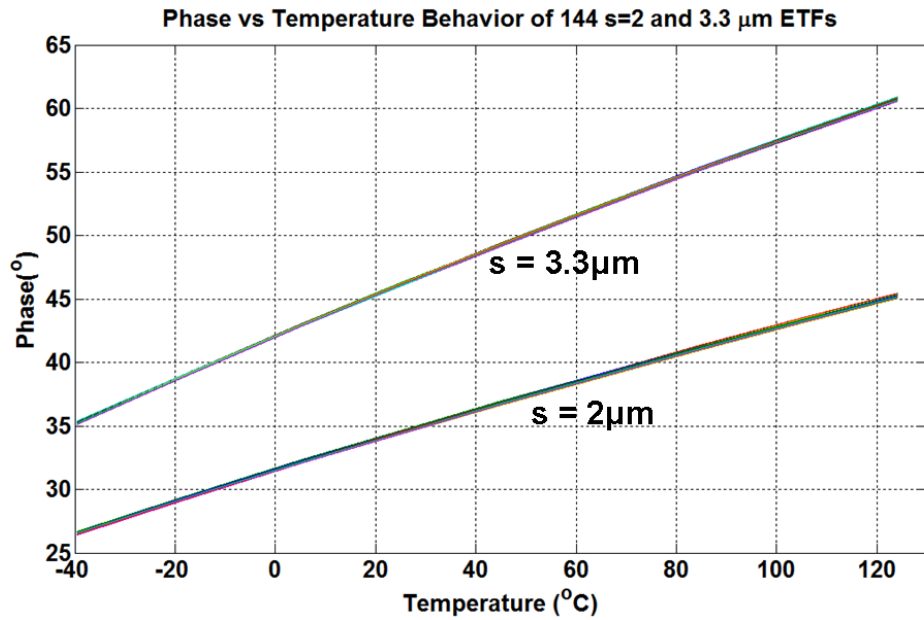


Fig. 9. Measured phase of  $s = 2\mu\text{m}$  and  $s = 3.3\mu\text{m}$  ETFs over temperature ( $F_{\text{DRIVE}} = 1.17\text{MHz}$ , 144 samples)

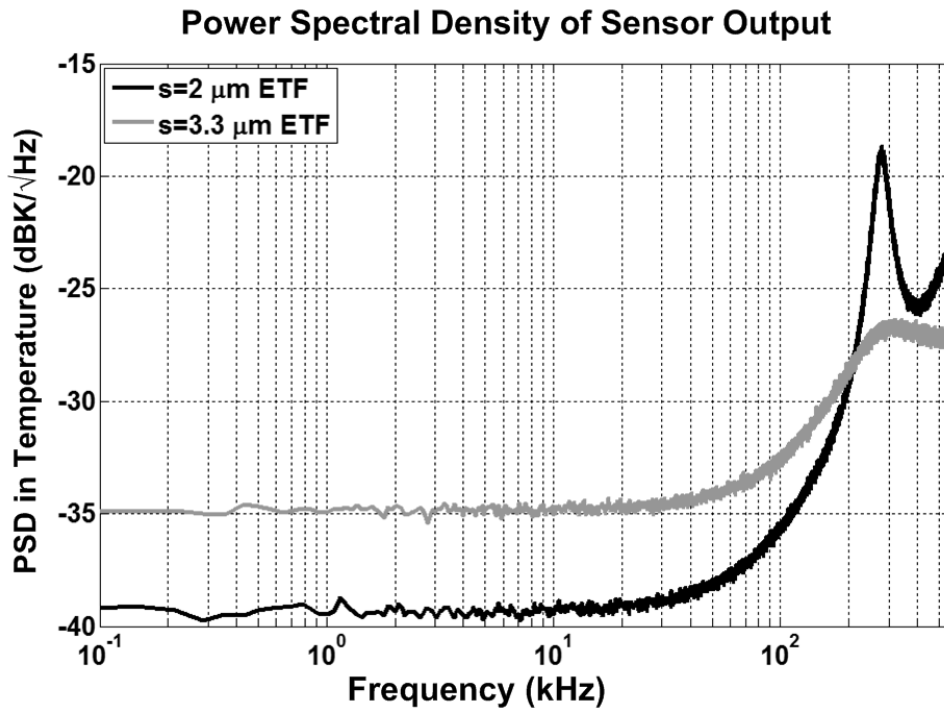


Fig. 10. PSD of the sensor's bitstream (8 million points,  $F_s = 1.17\text{MHz}$ )

### Phase Calibration Error over Temperature for 144 Readouts

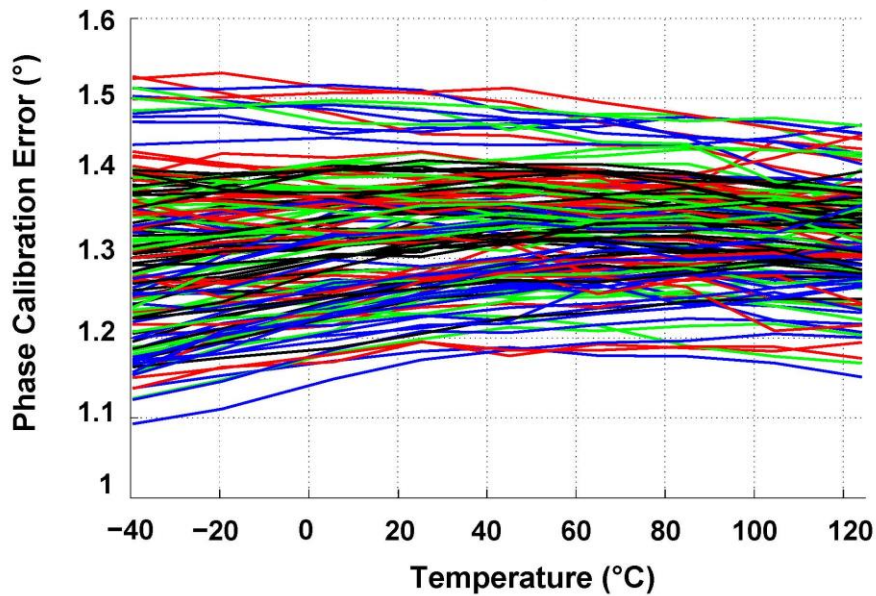


Fig. 11. Measured phase error of the readout circuitry of 144 sensors from -40 to 125 °C.

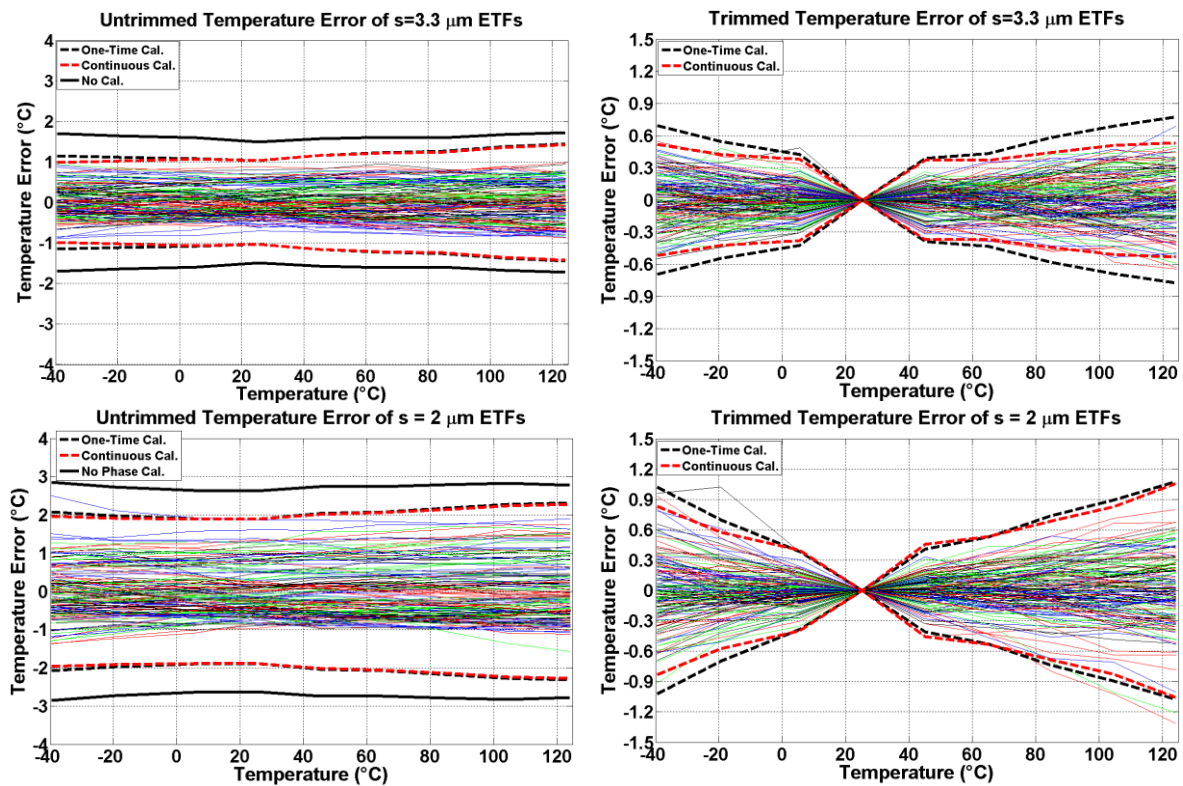


Fig. 12. Untrimmed and single-point trim inaccuracy for 144 sensors with  $s=3.3\mu\text{m}$  (top plots) and  $s=2\mu\text{m}$  (bottom plots). Individual lines represent the inaccuracy of each sensor with one-time phase cal., while the bold lines indicate the  $3\sigma$  limits for no phase cal., one-time phase cal. at 25 °C, and the red dashed lines represent continuous phase cal.

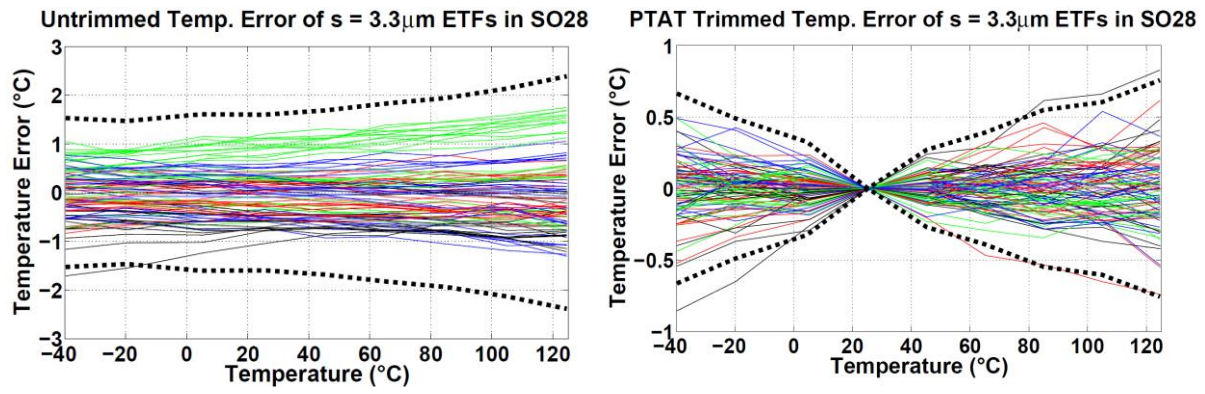
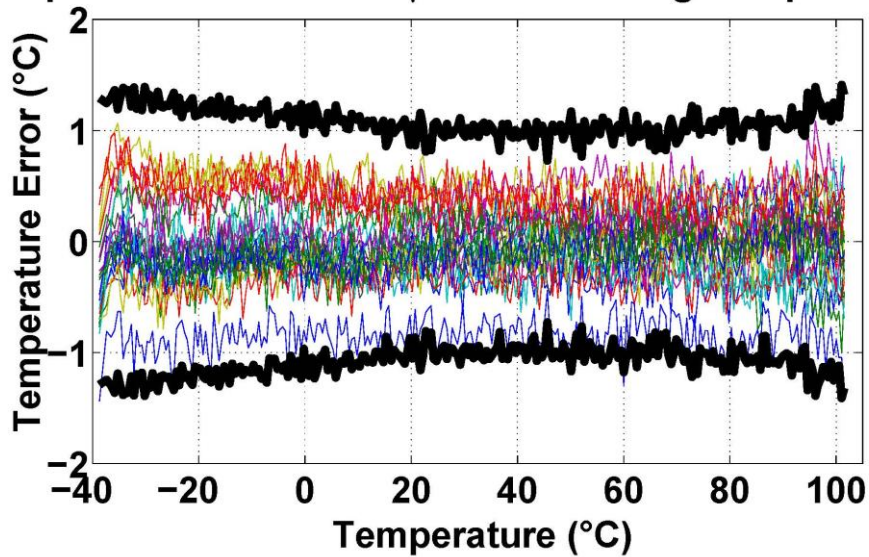


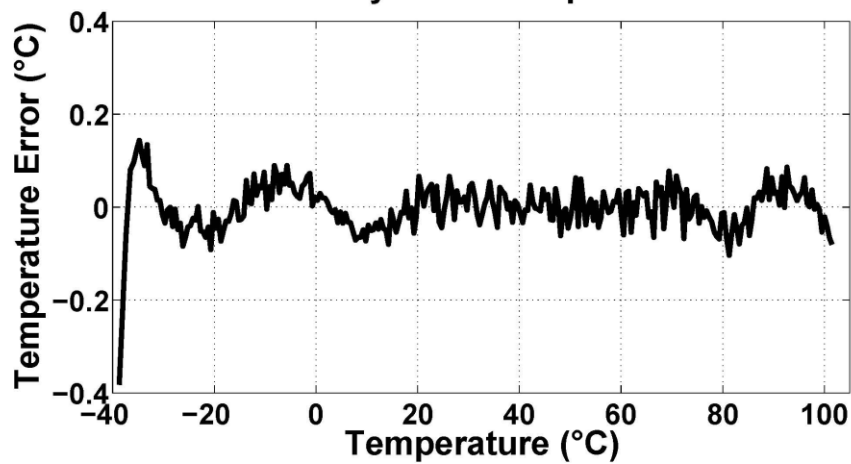
Fig. 13. Untrimmed and gain or PTAT trimmed inaccuracy for 96 sensors with  $s=3.3\mu\text{m}$ , in 16 SO28 plastic packages. Individual lines represent the inaccuracy of each sensor with one-time phase cal., while the dashed lines indicate the  $3\sigma$  limits for one-time phase cal. at 25 °C.

### Temp. Error of 24 s = 3.3 $\mu\text{m}$ ETFs During Ramp Meas.



(a)

### Mean Non-Linearity Error Compared to Oven Ramp



(b)

Fig. 14. (a) Temperature error of 24 sensors with 3.3- $\mu\text{m}$  ETFs during a ramped temperature test (50 mK/sample temperature slope, 1 kSa/s sample rate). Bold lines indicate  $3\sigma$  limits. (b) Non-linearity error between oven ramp and mean sensor output over temperature.

TABLE II. PERFORMANCE SUMMARY AND COMPARISON

	This Work		[13]	[15]	[5]	[4]	[26]	[27]	[14]
Technology	40nm		160nm	32nm	14nm	32nm	16nm	28nm	65nm
Sensor Type	TD (3.3 $\mu$ m)	TD (2 $\mu$ m)	TD (3.3 $\mu$ m)	Diode	BJT	BJT	BJT	BJT	MOS
Inaccuracy No Temp Cal. (3 $\sigma$ , °C)	$\pm 1.4$	$\pm 2.3$	$\pm 2.9$	-	$\pm 4.7$	$\pm 5$	$\pm 2.0$	$\pm 1.8$	-
Single Temp. Cal. (3 $\sigma$ , °C)	$\pm 0.75$	$\pm 1.05$	$\pm 1.2$	-	$\pm 2.3$	-	-	-	-
Two Temp. Cal. (3 $\sigma$ , °C)	-	-	-	$\pm 2.6$	$\pm 0.7$	-	-	-	$\pm 0.9^*$
Temp. Range (°C)	-40 to 125	-40 to 125	-35 to 125	0 to 100	0 to 100	-10 to 110	-50 to 150	-20 to 130	0 to 100
Area ( $\mu$ m <sup>2</sup> )	1650		2800 <sup>***</sup>	1000 <sup>**</sup>	8700	20000	12600	3800	4000
Resolution (°C, RMS)	0.36	0.24	0.47	0.25	0.5	0.15	0.38	0.58	0.3
Speed (kSa/s)	1		1	2.5	50	1.2	3.66	250	45
Supply Voltage (V)	0.9 – 1.2		1.8	1.65	1.35	1.05	-	1.1 - 1.8	0.85-1.05
Power (mW)	2.5		2.4	0.1	1.1	1.6	1.21	0.016	0.15
Resolution FoM (nJ·K <sup>2</sup> ) <sup>****</sup>	324	144	530	2.5	5.5	30	47	0.021	0.3

\* Peak to peak error variation (7 samples)

\*\* Area of precision voltage reference not included

\*\*\* Shared phase DAC area (~600  $\mu$ m<sup>2</sup>) not included

\*\*\*\* Resolution figure of merit (FoM) is defined as Power\*Conversion Time\*Resolution<sup>2</sup>

## LIST OF FIGURES

Fig. 1. Simplified layout of the proposed octagonal ETF in standard CMOS.

Fig. 2. Simple block diagram of a phase-domain  $\Sigma\Delta$  digitizing the phase output of an ETF.

Fig. 3. Block diagram of a VCO-based phase-domain  $\Sigma\Delta$ .

Fig. 4. Block diagram of the 3-bit VCO-based phase phase domain  $\Sigma\Delta$  modulator with phase calibration.

Fig. 5. Circuit diagram of the Gm-stage (cascaded CCO modelled as resistive load  $r_{CCO}$ )

Fig. 6. Circuit diagram of the CCO and the cascaded level shifter amplifier. The driving gm stage is modelled with its Norton equivalent ( $I_{CCO}$  current source and  $r_O$  output impedance).

Fig.7. Block diagram of the sensor digital logic for generation of  $F_{DRV}$  and  $F_{DEM}$  and truth table that describes the combinational logic function.

Fig. 8. Die photo, along with a zoomed-in photo of a single temperature sensor. The sensor's photo is showing the breakdown of area occupied by the ETF and circuitry.

Fig. 9. Measured phase of  $s = 2\mu\text{m}$  and  $s = 3.3\mu\text{m}$  ETFs over temperature ( $F_{DRIVE} = 1.17\text{MHz}$ , 144 samples)

Fig. 10. PSD of the sensor's bitstream (8 million points,  $F_s = 1.17\text{MHz}$ )

Fig. 11. Measured phase error of 144 sensor readouts from  $-40$  to  $125^\circ\text{C}$ .

Fig. 12. Untrimmed and single-point trim inaccuracy for 144 sensors with  $s=3.3\mu\text{m}$  (top plots) and  $s=2\mu\text{m}$  (bottom plots). Individual lines represent the inaccuracy of each sensor with one-time phase cal., while the bold lines indicate the  $3\sigma$  limits for no phase cal., one-time phase cal. at  $25^\circ\text{C}$ , and the red dashed lines represent continuous phase cal.

Fig. 13. Untrimmed and gain or PTAT trimmed inaccuracy for 96 sensors with  $s=3.3\mu\text{m}$ , in 16 SO28 plastic packages. Individual lines represent the inaccuracy of each sensor with one-time phase cal., while the dashed lines indicate the  $3\sigma$  limits for one-time phase cal. at  $25^\circ\text{C}$ .

Fig. 14. (a) Temperature error of 24 sensors with  $3.3\text{-}\mu\text{m}$  ETFs during a ramped temperature test (50 mK/sample temperature slope, 1 kSa/s sample rate). Bold lines indicate  $3\sigma$  limits. (b) Non-linearity error between oven ramp and mean sensor output over temperature.

## LIST OF TABLES

Table I. Noise, delay and power budgeting between ETF and readout blocks

Table II. Performance summary and comparison